RC23815 (W0511-178) November 28, 2005
Materials Science

IBM Research Report

Characterizing Probe Performance in the Aberration Corrected STEM

P. E. Batson
IBM Research Division
Thomas J. Watson Research Center
P.O. Box 218
Yorktown Heights, NY 10598

Research Division
Almaden - Austin - Beijing - Haifa - India - T. J. Watson - Tokyo - Zurich

LIMITED DISTRIBUTION NOTICE: This report has been submitted for publication outside of IBM and will probably be copyrighted if accepted for publication. Ithas been issued as a Research Report for early dissemination of its contents. In view of the transfer of copyright to the outside publisher, its distributionoutside of IBM prior to publication should be limited to peer communications and specific requests. After outside publication, requests should be filled only by reprints or legally obtained copies of the article (e.g, payment of royalties). Copies may be requested from IBM T. J. Watson Research Center , P. O. Box 218, Yorktown Heights, NY 10598 USA (email: reports@us.ibm.com). Some reports are available on the internet at http://domino.watson.ibm.com/library/CyberDig.nsf/home

Characterizing Probe Performance in the Aberration Corrected STEM

P.E. Batson

IBM Thomas J. Watson Research Center,

Yorktown Heights, NY 10598, USA

(Dated: November 4, 2005)

Abstract

Sub-Angstrom imaging using the 120kV IBM STEM is now routine if the probe optics is carefully controlled and fully characterized. However, multi-slice simulation using at least a frozen phonon approximation is required to understand the Annular Dark Field image contrast. Analysis of silicon dumbbell structures in the [110] and [211] projections illustrate this finding. Atomic movement is ubiquitous under the electron beam and, using fast image acquisition, can illuminate atomic level processes that might be missed in still images.

Keywords: aberration correction, quadrupole-octupole corrector, scanning transmission electron microscopy.

PACS numbers: 07.78.+s , 61.16.Bg

I. INTRODUCTION

In an earlier report, we showed that sub-Angstrom probe sizes are possible at 120 KeV electron energy using aberration corrected optics. [1, 2] This performance at a relatively low accelerating voltage promises to allow detailed atomic level analytical measurements in radiation sensitive semiconductor nanostructures. At IBM, my interest is in direct measurement of electronic and optical properties that can aid understanding of device operation. For instance, measurement of the damping parameter for plasmons, or core losses in confined volumes can provide information about the local conductivity. [3, 4] Measurement of core loss fine structure in device gate isolation oxides is also directed towards this goal. [5] With the continuing progress towards ever smaller device structures, measurement using sub-Ångstrom resolution and positional accuracy is rapidly becoming a requirement for successful device development. To this purpose, this instrument is intended to deliver both sub-Angstrom spatial resolution and 100meV EELS energy resolution using a monochromator and high resolution spectroscopy.

II. SUMMARY OF THE DEVELOPING SYSTEM

The IBM instrument is a VG Microscopes HB501 STEM, fitted with the first Nion quadrupole-octupole aberration corrector.[6] Figs. 1,2 summarize the current mechanical configuration. Since it is intended to address electrical properties in semiconductor devices, it was fitted with a high resolution spectrometer in 1986. [7] The power supplies for this instrument have recently been upgraded to allow operation of the spectrometer in the 50-150meV resolution level. The Nion corrector, as described elsewhere, is positioned between the double condenser and objective lens. [6] A gun monochromator has been constructed and has been demonstrated to deliver an energy spread of better than 50 meV while preserving the gun brightness. [8] When used together with the existing spectrometer, a spectral resolution of 50-100meV should be possible using the sub-Ångstrom probe. Presently, it is possible to produce a sub-Å probe with a beam current of 150pA. Modification of the spectrometer coupling optics currently allows 100-130meV spectrometer resolution using a specimen acceptance half angle of 10 mR.

In addition to the above major changes, conversion of the VG STEM to a very high

resolution instrument has required many very minor but basic changes. For instance, a belt reduction drive has been added to the specimen mechanical shifts to produce a finer mechanical step, and the shift and tilt indicators are digitally measured to provide numerical readouts. These changes, which allow reproducible mechanical positioning at the 10 nm level, have substantially reduced the time required to tune the microscope aberrations by making large specimen shift and tilts more systematic. These are required to move between the microscope alignment specimen and the semiconductor area of interest. Routine atomic level image movement has required image acquisition at 5-10 frames per second, allowing investigation of dynamic processes in the microscope. Although Selected Area Diffraction was initially lost on addition of the aberration corrector, it has been found possible to regain this behavior by refocussing the aberration corrector to obtain a stigmatic focus at the back focal plane of the objective lens. If this is done carefully, it can be accomplished without grossly damaging the corrector conditions for the sub-Å probe. The relatively stiff VG Microscopes vibration isolation was replaced with a passive air bearing system. This performs well at frequencies above its 2.5 Hz resonance, but will require active damping to isolate against very low frequency floor vibration.

III. REPRODUCIBILITY OF THE PROBE OPTICS

Perhaps the biggest operational change on going to aberration corrected systems lies in the complexity required to describe and control the electron beam. In the past, two to four optical parameters – defocus, spherical aberration, astigmatism and sometimes coma – were adequate to model images. With the first generation Nion corrector we have the ability to measure up to fifth order in aberrations, (about 25 coefficients), and accurately control up to third order (12 coefficients). Krivanek has suggested a nomenclature for keeping track of these. We define a phase shift $\chi(\vec{k})$ for an electron wavefront in a lens back focal plane, with $\vec{k} = (k, \phi)$ where ϕ is an azimuthal coordinate, and k is a radial wavevector for the probe electrons. We can then specify this phase shift in terms of aberration coefficients: [2]

$$\chi(k,\phi) = K_0 \sum_n \frac{(k/K_0)^{(n+1)}}{(n+1)} \sum_{m+n\ odd,\ m<n+1} \left[C_{nma}\ \cos(m\phi) + C_{nmb}\ \sin(m\phi)\right]. \qquad (1)$$

In this expression, the scattering angle $\theta \simeq k/K_0$ where K_0 is the wavevector of the incident electrons. In this aberration numbering scheme, coefficients are identified by subscripts: the first giving the exponent for the radial wavevector (or angle) for the aberration, the second its axial symmetry and the letter indicating the orientation of the axial symmetry. Thus C_1 defines defocus and $C_{12a,b}$ denotes astigmatism; coma, which is second order in angle, becomes $C_{21a,b}$ and C_3 identifies spherical aberration.

The probe wavefunction can then be written:

$$\Psi_p(\vec{r}) \propto \int_{aperture} \exp\big[\, -i\chi(\vec{k}) \;-\; i\vec{k}\cdot\vec{r}\,\big] d\vec{k} \tag{2}$$

where the probe amplitude is given as a function of the real space coordinates $\vec{r}$. This expression is a generalization of the standard result [9] for an optical system that does not have axial symmetry. Eqs. 1 and 2 provide a prescription for calculating the size and shape of the probe given a set of aberration coefficients. Inclusion of chromatic aberration is done by summation of probe intensities for different defocus values weighted by the electron beam energy distribution, $\rho(E)$.

$$|\Psi_p(\vec{r})|^2 \;=\; \int |\Psi_p(\vec{r}, C_1(E))|^2 \, \rho(E) dE \tag{3}$$

For the calculated chromatic aberration, C_c of 1.7 mm for the VG Microscopes, $C_s = 1.3\,mm$, high resolution pole piece, this contribution is unimportant to the result. Finally a source size contribution of 0.03-0.05 nm is included by convolution of the result with a guassian distribution.

In earlier reports, Krivanek and Dellby, [6, 10] and Lupini [11] have detailed a method for obtaining these coefficients based on evaluation of out of focus electron shadow maps, or Ronchigrams, using 5-10 nm gold islands on a carbon support as an object. Use of shadow maps for characterization of optical systems was extensively discussed by Ronchi [12] and more recently by others for electron beams. [13] In practice, these maps provide image plane shifts as a function of angular displacement in the objective lens, which can be used to derive aberration parameters. When the Ronchigram is taken at probe focus, we obtain a pattern that is essentially a microdiffraction pattern and is strongly related to the integrand in Eq. 2

above. Thus: [11]

$$\mathcal{R}(\vec{k},\vec{r}_0) \propto \int \mathcal{T}(\vec{r})\Psi_p(\vec{r}-\vec{r}_0)\ \exp(i\vec{k}\cdot\vec{r})d\vec{r} \tag{4}$$

where the Ronchigram amplitude, $\mathcal{R}(\vec{k},\vec{r}_0)$, is obtained from the Fourier transform of the specimen transmission function, $\mathcal{T}(\vec{r})$, multiplied by the probe wavefunction. The observed intensity is, of course, $|\mathcal{R}(\vec{k},\vec{r}_0)|^2$. To calculate this for an amorphous thin film, I use a Phase Object Approximation for the specimen function:

$$\mathcal{T}(\vec{r}) \ = \ \exp\bigl[-i\sigma R(\vec{r})\bigr] \tag{5}$$

where $R(\vec{r})$ is a random amplitude generator having a characteristic length scale of about 0.25 nm and a maximum amplitude of 1. I have arbitrarily set the scattering cross section, σ, to 0.1 for an easily observable contrast. For each microscope setup, it is therefore possible to obtain aberration coefficients and to use these to calculate both the probe intensity and the in focus Ronchigram appearance for comparison with measurements. This improves over a qualitative estimate for the Ronchigram shape that I used in the previous publication.[2] Finally, we can simulate an annular dark field image of a single Au atom using the multislice technique, and compare this with measured atom images to decide how well the optical system is described by the measured parameters.

Fig. 3 and Table I summarize results required to support the discussion above. Measured aberrations up to fifth order are shown in the table. Typical values for C_5 are in the range 1.5-6.5cm, while the two-fold and four-fold fifth order distortions are 2-5x smaller. Target values for low order aberrations are chosen to offset the fourth and fifth order measured values. So, for instance, target values for coma (C_{21ab}) are optimized to partially offset fourth order coma ($C_{41a,b}$) within the objective aperture. Target values for these are derived in much the same way that the Scherzer defocus is obtained in the uncorrected systems. In Fig. 3a, the Ronchigram intensity using Eq. 4 is shown for this set of aberrations consisting of the target values up to and including coma, and the measured values for all higher orders. This process recognizes that the lower order coefficients are adjusted by hand during imaging to correct inaccuracies introduced by instabilities – mainly floor vibration – which produces unacceptable scatter in the measurements for the low orders. Fig. 3b shows an image of the in focus Ronchigram taken soon after the aberration measurement for comparison.

Numerical investigation shows that the apparent pseudo-five-fold azimuthal symmetry in this case is caused by a large 4th order coma, C_{41b}. Fig. 3c shows the calculated intensity for a single Au atom for comparison with the Au atom measured image in Fig. 3d. Fig. 3e shows line scans for the Au projected potential, the probe intensity, and an ADF atom image calculated for a 25 mR half angle objective aperture. These can then be compared with experimental single atom images as shown in Fig. 3f. It is only after this exercise that we are confident that the probe parameters are well understood, and can later be used to help interpretation of experimental images.

The experimental atom line scans are a little broader than the predicted curves and have extended tails. It is likely that the FWHM can be affected by an incorrect estimate for the source size contribution. But the probe tails are harder to understand. It is known that chromatic aberration can produce probe tails, but we believe that this should be negligible in this instrument. An incorrect defocus can also contribute to probe tails,[14] and so this points out the need for an objective method for accurately focussing the instrument during imaging, or by providing a means to measure defocus in each image. This has been done in sub-Ångstrom bright field TEM work by adding a thin carbon layer to the specimen exit surface, appropriate for Thon ring analysis.[15]

The precise value for the source size contribution turns out to be difficult to determine and to control because the simple three element gun-accelerator design in the VG instrument produces large magnification variations for small variations in the separation between the tip and the first anode. Fig. 4 shows results from a calculation of the optical properties for the VG gun. No attempt was made here to model the fields in the immediate region of the tip, so this calculation does not give an estimate of the absolute value of the source contribution. But it does describe the optical properties of the extraction and acceleration fields to estimate the effects that changes in fields or gun geometry will produce. It is apparent that the magnification of the source is a sensitive function of both the tip extraction field and the tip-anode separation, and can change by a factor of 1-5x using typical values. The tip-anode separation in particular is not well controlled, probably because it was never a limitation of performance at the 0.2 nm level and above. The Figure makes clear that the source size contribution can be made small by minimizing the tip-anode distance and by working at a high extraction field. This last condition, particularly, contradicts a longstanding belief that the best performance in the VG instrument is obtained using a sharp tip operating at

low extraction fields. While this calculation has been done for 120 kV operation, a similar conclusion is obtained at 100 kV. To illustrate the importance of this finding, I plot two well characterized situations labeled by their corresponding measured probe sizes.

Detailed image characterization in the 100 keV uncorrected system estimated the source size contribution at the specimen to be about 0.7 Å.[16] In that case, optical demagnification above the gun was of order 20-50x. In the corrected system this demagnification has been increased to about 100x. Therefore, an estimated source size contribution in the present case of about 0.2-0.4 Åseems reasonable. It is therefore very clear that a factor of even 2x degradation of this due to gun setup would limit the performance of the whole system.

In principle, source magnification by the gun optics should be correctable using additional demagnification in the condenser lenses. I have found this to be difficult in practice, partly because the beam defining aperture lies between the condenser lenses and the gun. Therefore changes in demagnification affect the apparent size of this aperture, requiring different physical aperture sizes for different demagnification values. Also, with this generation corrector, the ultimate probe size is limited by the value of the 5th order combination aberrations, which are the result of incorrect coupling of the corrector image planes with the objective lens.[6] These types of aberrations can be reduced by increasing the size of the beam within the corrector, effectively increasing the demagnification between the corrector and the objective lens, further restricting the acceptable operating ranges of the condenser lenses. Finally, for the larger tip/1st anode distances, quite a large fraction of the beam current is intercepted by the 1st anode, requiring larger extraction currents to produce comparable beam current. I have found that lowering the tip by 0.4 mm can double the 1st anode current for the same beam current. This behavior can contribute to shortened tip lifetimes. In order to mitigate this, I have modified the tip assembly to allow about ± 0.25 mm adjustment of the tip height during installation. When the monochromator is installed, this experience will be valuable for optimization of the source size.

IV. ASSESSMENT OF RESOLUTION

While the discussion above demonstrates the sub-Ångstrom probe size, a practical characterization of spatial resolution depends strongly on 1) the *shape* of the probe – does it have sharp features, 2) the relationship of the specimen object function to the real structure of

the specimen, and 3) the measurement quality – to what extent are spatial features obscured by a random noise background. Consideration of these issues leads to a realization that no one number can be used to summarize the spatial resolution of an instrument. Nor is the concept of resolution a very good way to think about a particular measurement. A better way to approach this problem is to ask how to interpret a set of measurements in terms of a model structure. Then it becomes clear that the accuracy of such an interpretation depends on an assessment of each of the above issues.

A convenient way to approach this is by use of the Contrast Transfer Function, (CTF) which summarizes the visibility of specimen structure as a function of the spatial frequencies which define it. This has been discussed extensively for ADF imaging by Loane, et al.[14] In the incoherent imaging model, the Annular Dark Field (ADF) STEM image can be described by a convolution of the probe intensity with a specimen object function, which may or may not be linearly related to the real specimen structure. This model separates resolution issues related to shape of the probe from those which are related to the specimen: thickness, orientation, crystallinity, etc. In this case, the CTF is simply the fourier transform of the probe shape. Fig. 5 summarizes the CTF for the probe conditions from the above discussion about optical reproducibility. This figure presents axially averaged CTFs for the conditions above (full line) and for a second, comparable setup (dashed line). These are compared with CTFs derived from the corresponding Au atom images (open and closed circles). The large data points were derived from zone axis imaging of Si and will be described below. This illustration shows that we expect to obtain a fringe contrast level of somewhere between 0.5-2 % at 0.8 Å. Information should be present out to the limit of the probe forming aperture – about 0.68 Å– because this system is not limited by chromatic aberration. Whether or not this information is useful depends on the noise level in the measurement, which obscures contrast smaller than this noise level.

In general, ADF STEM imaging provides a useful, directly interpretable image because the CTF is positive (atoms are always bright), and monotonically tends to zero at large spatial frequencies. It is also non-zero at zero frequency, so it is sensitive to differences in average scattering over long distances. This presents a problem when a material containing strongly scattering atoms lies near structures composed of light atoms. Then, the strong contrast from the heavy material can interfere with our ability to obtain, to display and even to interpret structure in the light atom matrix. On the other hand, the non-zero CTF

at low frequencies provides an advantage over aberration corrected BF TEM imaging, which suffers from a widening of the low frequency region of low contrast as spherical aberration is pushed towards zero. This can obscure object features which are intermediate in size, affecting interpretation of the object structure on the 1-5 nm level.

V. COMPARISON OF RESULTS WITH MULTISLICE SIMULATIONS

It is well known that BF TEM measurements require comparisons with multislice image simulations for understanding. ADF STEM imaging at the sub-Angstrom level also requires this. As discussed above, image contrast is not only controlled by the probe shape, but is sensitive to details of the probe propagation through the specimen. In Fig. 6, I summarize frozen phonon multislice ADF image simulations for the Si [110] and [211] projections. I follow Kirkland [9] for the general calculation method and use his projected atomic potentials. However, the details of the calculation differ somewhat, following more closely techniques needed for amorphous objects. (See for instance, [17]) The main features of this method are: 1) an area anchored to the beam position defines a multislice calculation region wherein periodic boundary conditions are applied; 2) each layer structure is specified as needed using that part of a larger model structure that lies within that area, suitably perturbed by the frozen phonon shifts. The method allows one to minimize the calculated region for thin specimens in order to make the calculation time as small as possible. In the figure, the upper images show intensity distributions across the dumbbell structures in the [110] and [211] projections as a function of thickness to a maximum of 20 nm. Excepts from these results for 0.4, 10 and 20 nm are shown at the bottom. The initial probe wavefunction was calculated using the first, third and fifth order coefficients as shown in Table I. The ADF scattering intensity was integrated over a range from 60-300 mR. A source size of 0.05 nm was convoluted with the multiple scattering results for the final curves. The phonon amplitude was 0.0078nm. [16]

We can see that the dumbbell contrast decreases markedly in the [110] case, but appears relatively constant for the [211] case as a function of thickness up to 20 nm. The decrease in contrast is caused by the tendency of the beam to shift into the potential well which surrounds an atomic column. This means that a small probe which is initially placed between two closely spaced columns can quickly move onto the adjacent columns, producing higher

ADF scattering and reducing the dumbbell contrast. This possibility has been noted by others, also. [18] In thick sample regions, the beam will oscillate among several columns depending on details of the extinction distance and diffraction conditions. Studies of this type show how well the specimen object function resembles the real specimen structure – in this case not too badly – but inspection of the propagation of the probe provides a strong caution against simple interpretation of analytical results based on the appearance of the ADF image. This particular study also points out that the 0.78 Å dumbbell in the Si [211] projection is actually easier to detect than would be expected based on a simple convolution of the probe with the projected potential of the specimen – a situation summarized in the top plot of Fig. 6.

In Figs. 7 and 8, I compare image data and line scans with multislice results for several directions in the Si [110] and [211] projections. The images here were obtained in single 0.2 sec exposures of areas which were several times larger than shown in the images. About a dozen patches from these exposures were then aligned by cross correlation and added together to obtain good quality statistics. This process removed most of the image distortion caused by floor vibration mentioned above. The images were subjected to a low pass filter with a cutoff of 0.02 nm to reduce the displayed noise, but similar results were obtained with a simple 4x4 binning of the data.

It can be remarked at first that the comparison of results with calculations is very favorable. For the most part the relative contrast for various fringe spacings matches the calculation closely. For the purpose of comparison with the expected CTF, I matched the measured contrast of the lowest frequency fringe in each image with the expected value from the CTF. Then I used the visibility of other fringes relative to these to place experimental points in Fig. 5. Clearly the observed contrast for these small features compares well with our expectations, even for the very short 0.78 Ådistance. It is also clear from that figure that we would not be able to image that feature size if the measurement noise were higher than about 1%. The trade off between resolution and measurement noise is very stringent in this case, where the fringe spacing is nearly the same as the FWHM of the probe. This result also illustrates that in order to obtain high contrast values, the probe width should be of order 2x smaller than the fringe spacing – a condition probably strongly related to the Nyquist-Shannon information sampling limits.

It is also clear from these results that the detailed Si [004] dumbbell fringe is not very well

reproduced by the calculation, unless a 0.08 nm source size is used, and even then the fit is not very satisfying. However, this source size is not consistent with the [211] results, because in that case the [444] fringe would not be visible, as summarized in Fig. 8. One possible explanation for this is that, particularly near these limits in a prototype instrument, there may be variations in optical setup from day to day that could produce these differences. I have compared several results from the past couple years, including results using different FEG sources, hunting for this possibility. In each case where I can verify the imaging conditions as described above, these results are typical.

I am going to speculate, therefore, that this is a real measurement of some specimen quantity that differs from our expectation. I suggest that crystallographic anisotropy in the phonon vibrational spectra may be responsible. We know that silicon is of order 100x stiffer in the [111] direction (bond stretching) than it is in the [001] direction (bond bending), with the [110] direction somewhat intermediate between the two extremes. [19] This behavior has been investigated in the simulation of zone axis patterns in Si by Muller. [17] In this case, we expect [444], [111] and [022] directions should be well characterized by the average phonon displacement of 0.0078 nm. The [004] direction, however, will be subject to higher displacements, resulting in blurring in that direction that is an accurate reflection of the vibrational motion of the Si atoms.

VI. IMAGING HF ATOMS IN HI-K DIELECTRIC STRUCTURES

What is the practical result for this level of resolution? Fig. 9 shows a BF-ADF image pair of a structure consisting of poly-Si, HfO_x, and SiO_x on a silicon substrate. The first thing to note is that both images display a wealth of high contrast features. Using larger probes, the BF STEM signal has not been very helpful in the past. With the aberration corrected probe, the BF signal can be used for a quick assessment of crystallinity over large areas. Next, we can see that the ADF signal also shows a wealth of fringes associated with crystallinity. Again, using larger probes, there were only a very limited set of lattice spacings that were accessible. So lattice images were restricted to well oriented low index planes. Using the sub-Ångstrom probe, lattice fringes are everywhere.

As noted above, a mixture of high and low atomic number atomic species usually leads to contrast problems: low number atoms are swamped by the strong scattering of the high

atomic number atoms. This does not need to be the case for this probe size, provided the thickness is kept small. In this case, the probe can propagate between atom columns, even for the hi-Z material, providing a low background field, against which to view the light atoms, even within 1 Å of the heavy material. Therefore, the ADF image in Fig. 9 gives a faithful representation of the atomic number density that the beam encounters.

In this example, we can see several interesting features: 1) Hf atoms are present within the SiO_x; 2) they exhibit a distribution that can be measured; 3) they can also be imaged individually; 4) while they in general favor a location proximate to the Si, they do not appear to approach the Si closer than about 3 Å; and 5) they are rapidly moving under the STEM probe. Fig. 10 summarizes five images using 0.2 sec integrations, obtained at 1 sec intervals. The sequence shows that during the beam illumination, a cluster of Hf atoms migrates towards the Si substrate – essentially turning a Hf asperity (arrows), pointed at the HfO_x, into a relatively uniform layer next to the Si. This layer is not very dense, amounting to less than 5% by number relative to the SiO_x. While this movement is beam driven, it is not too difficult to show that the energy given up by the direct impact of a 120 kV electron with a Hf atom is probably less than 1 eV, so the process shown here is not too energetically different from that which may be driven thermally under high temperature processing conditions.

Finally, it must be noted that this movement requires a rapid acquisition in order to faithfully summarize the behavior of this material. An exposure time of even 10 sec would reveal only the final equilibrium positions. In addition, observation of large displacements between frames suggests that there are probably even faster motion occurring. It seems certain that this behavior must also occur in other instruments, but this appears to be the first systematic identification of it. It is possible that the low energy, high current nature of this instrument enhances atomic movement. But on the other hand, the current density of order $3x10^6$ A/cm^2 is only about 2x bigger than that present in the original 2 Å instrument, so it would seem that this would not be the case.

VII. SUMMARY

This discussion shows that it is possible to characterize the STEM optics well enough that detailed comparisons may be made between experimental images and multislice calculations,

and that these calculations are needed to understand the experimental results. The probe size can be verified in this exercise, and an estimate of the achievable resolution in the presence of measurement noise and dynamical scattering can be obtained. The image detail, even at 120 kV, can be strongly sub-Ångstrom, showing very high contrast and single atom detectability within the bulk of a semiconductor nano-layer. The ability to do this using the low acceleration voltage is very useful, possibly crucial, for application to radiation sensitive semiconductor materials. This work also suggests that there are still some problems in interpretation which may be related to modeling of vibrational motion of atoms in the bulk.

I wish to acknowledge extensive collaboration with O.L. Krivanek and N. Dellby who are responsible for this corrector design and construction. I also am indebted to J. Silcox for many years of support and advice.

---

[1] P.E. Batson, Niklas Dellby, and O.L. Krivanek, Nature **418**, 617 (2002).

[2] P.E. Batson, Ultramicroscopy **96**, 239 (2003).

[3] P.E. Batson, Sol. St. Comm. **37**, 477 (1980).

[4] P.E. Batson and J.R. Heath, Phys. Rev. Lett. **71**, 911 (1993).

[5] D.A. Muller, T. Sorsch, S. Moccio, F.H. Baumann, K. Evans-Lutterodt, and G. Timp, Nature **399**, 758 (1999).

[6] N. Dellby, O.L. Krivanek, P.D. Nellist, P.E. Batson, and A.R. Lupini, J. Electron Microscopy **50**, 177 (2001).

[7] P.E. Batson, Rev. Sci. Inst. **57**, 43 (1986).

[8] H.W. Mook and P. Kruit, Ultramicroscopy **81**, 129 (2000).

[9] E.J. Kirkland, *Advanced computing in electron microscopy* (Plenum Press, New York, 1998).

[10] O.L. Krivanek, N. Dellby, and A.R. Lupini, US Patent Application (unpublished).

[11] A.R. Lupini, *Dissertation* (Cambridge University, ADDRESS, 2001).

[12] V. Ronchi, Applied Optics **3**, 437 (1964).

[13] J.A Lin and J.M. Cowley, Ultramicroscopy **19**, 31 (1986).

[14] R.F. Loane, P. Xu, and J. Silcox, Ultramicroscopy **40**, 121 (1992).

[15] C. Kisielowski, C.J.D. Hetherington, Y.C. Wang, R. Kilaas, M.A. O'Keefe, and A. Thust, Ultramicroscopy **89**, 243 (2001).

[16] J. Silcox, P. Xu, and R.F. Loane, Ultramicroscopy **47**, 173 (1992).

[17] D.A. Muller, B. Edwards, E.J. Kirkland, and J. Silcox, Ultramicroscopy **86**, 371 (2001).

[18] C. Dwyer and J. Etheridge, Ultramicroscopy **96**, 343 (2003).

[19] J. Wang, K. Zhang, and X. Xie, Sol. St. Comm. **86**, 731 (1993).

Coefficient	Name	Measured(nm)	Target(nm)
C_1	Defocus	-1992	0.84
C_{12a}	Astig	-4.7	0.37
C_{12b}	Astig	14.5	0.05
C_{21a}	Coma	821.4	30.8
C_{21b}	Coma	-454.8	-373.6
C_{23a}		-64.9	-48.3
C_{23b}		-70.2	-97.3
C_3	Cs	-21683.1	-19944.8
C_{32a}		-7047.1	-6627.2
C_{32b}		-1065.4	-871.0
C_{34a}		-7171.3	-6561.3
C_{34b}		7559.0	6953.3
C_{45a}		23257	$\cdots$
C_{45b}		14581	$\cdots$
C_{43a}		157647	$\cdots$
C_{43b}		317776	$\cdots$
C_{41a}		-100744	$\cdots$
C_{41b}		1219987	$\cdots$
C_5		44036570	$\cdots$
C_{56a}		-574852	$\cdots$
C_{56b}		4764472	$\cdots$
C_{54a}		18663131	$\cdots$
C_{54b}		-19778172	$\cdots$
C_{52a}		14083539	$\cdots$
C_{52b}		1851017	$\cdots$

TABLE I: Typical measured aberrations compared with optimum tuning aberrations up to 3rd order to produce the best probe. Defocus, astigmatism and coma (C_0, C_1a, b and $C_2 1a, b$) are not auto-tuned, but adjusted by hand during imaging.

Figure 1. Line drawing of the IBM VG STEM. The Nion aberration corrector has replaced the VG scan coils, between the condensor and objective lenses. A CCD TV camera located just below the spectrometer obtains convergent beam diffraction information for Ronchigram measurement of objective lens aberrations. An electron monochromator has been designed and built for the gun, but has not yet been operated with the aberration corrector. Extensive changes to the spectrometer coupling optics and CCD detection system have been made to allow 50-150 meV energy resolution with the sub-Angstrom probe.

Figure 2. The IBM VG STEM was delivered in 1982 for materials studies in semiconductors. The upper chamber contains a Wien filter spectrometer for high resolution EELS measurements. The microscope is supported on an air bearing system to isolate it from floor vibration, and is located within a shielded room to reduce AC magnetic field interference.

Figure 3. A summary of comparisons between calculated and experimental tests which verify correct operation of the aberration corrected system. a) calculated Ronchigram intensity with dashed line indicating extent of 50mR diameter objective aperture, b) measured Ronchigram through a 140mR diameter aperture, c) calculated ADF gold atom image intensity, d) measured ADF image of a single Au atom, e) calculated line scans for the gold atom potential, the probe, and a gold atom ADF image, f) line scan measurements of the Au atom intensity along perpendicular directions.

Figure 4. Source magnification as a function of extraction voltage and separation between the tip and first anode for the VG Microscopes gun. Tip height variations as small at 0.2 mm can affect the source size by large amount for the lower extraction voltages.

Figure 5. Contrast Transfer Function for linear ADF imaging using the 0.8 Å diameter probe at Guassian focus. Clearly only a small part of the total contrast information is useful for answering questions about structure on the 0.8 Å length scale. Circles are measurements of contrast in Si [110] and [211] projections.

Figure 6. Comparison of multislice ADF image calculations for the dumbbell structures in the Si[110] and [211] projections as a function of specimen thickness. In the [110] case,

the dumbbell contrast decreases as the thickness increases, while the [211] dumbbell contrast remains relatively constant.

Figure 7. Image and line scan data from Si[110], compared with multislice simulations using 0.05 and 0.08 nm source sizes. Agreement is good for the [111] and [220] type fringes at 0.05 nm source size, but the dumbbell [004] fringes are not well characterized by the calculation.

Figure 8. Image and line scan data from Si[211], compared with multislice simulations using 0.05 and 0.08 nm source sizes. Agreement is good for both the [220] and the 0.78 Å[444] dumbbell fringes using a 0.05 nm source size. However, the [444] finges would not be resolved using a 0.08 nm source.

Figure 9. BF-ADF image pair of a hi-K dielectric structure. Hf atoms within the SiO_x interface layer are readily visible in the ADF image. The images were acquired for 0.2 sec using a beam current of order 150 pA..

Figure 10. ADF images of Hf atoms within the SiO_x interface layer between HfO_x and Si substrate of a hi-K gate insulator structure. The images were integrated for 0.2 sec at intervals of 1 sec.

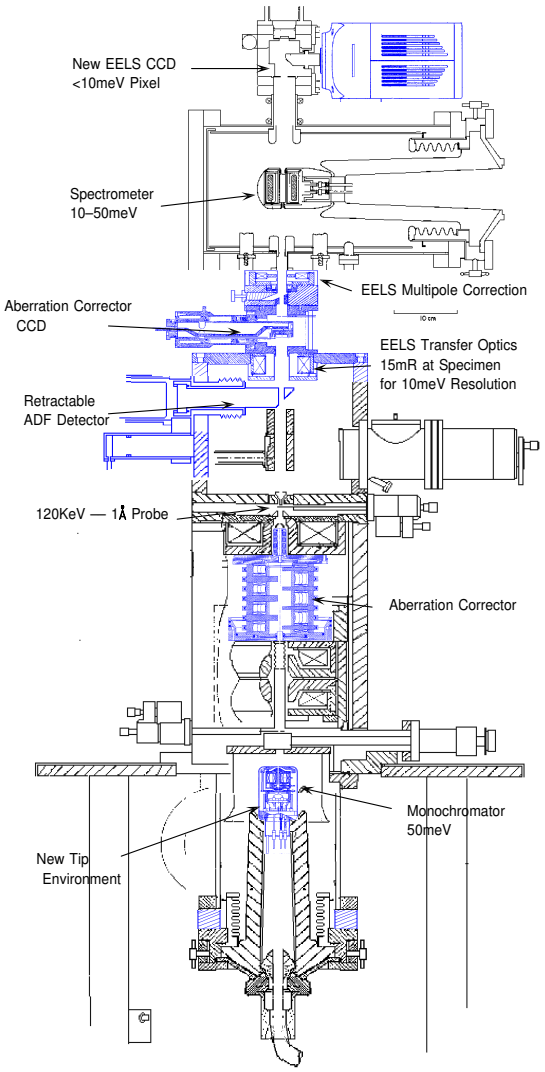

FIG. 1: Line drawing of the IBM VG STEM. The Nion aberration corrector has replaced the VG scan coils, between the condensor and objective lenses. A CCD TV camera located just below the spectrometer obtains convergent beam diffraction information for Ronchigram measurement of objective lens aberrations. An electron monochromator has been designed and built for the gun, but has not yet been operated with the aberration corrector. Extensive changes to the spectrometer coupling optics and CCD detection system have been made to allow 50-150 meV energy resolution with the sub-Angstrom probe.

FIG. 2: The IBM VG STEM was delivered in 1982 for materials studies in semiconductors. The upper chamber contains a Wien filter spectrometer for high resolution EELS measurements. The microscope is supported on an air bearing system to isolate it from floor vibration, and is located within a shielded room to reduce AC magnetic field interference.

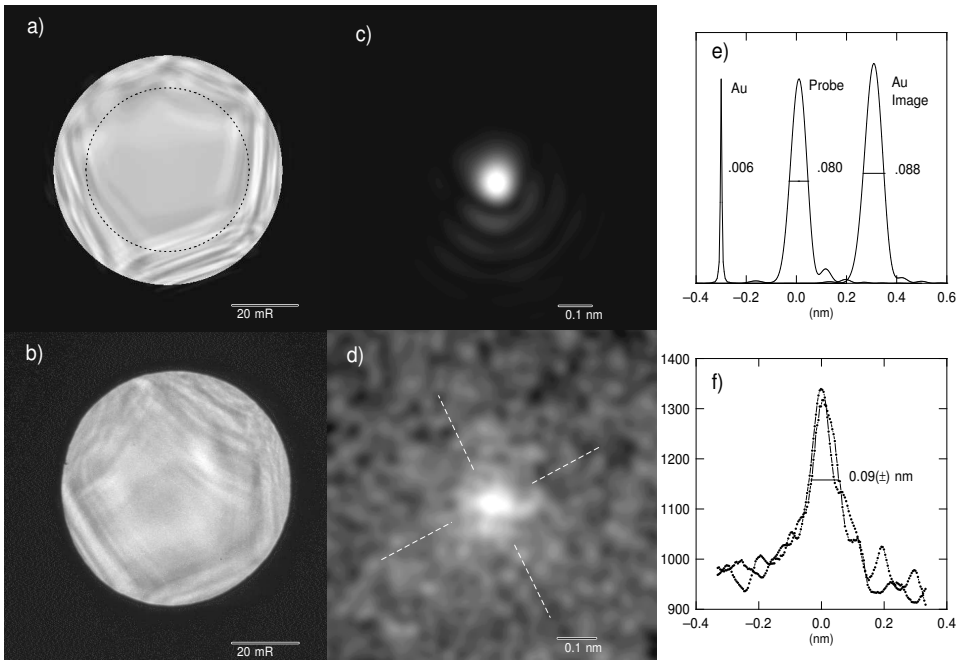

FIG. 3: A summary of comparisons between calculated and experimental tests which verify correct operation of the aberration corrected system. a) calculated Ronchigram intensity with dashed line indicating extent of 50mR diameter objective aperture, b) measured Ronchigram through a 140 mR diameter aperture, c) calculated ADF gold atom image intensity, d) measured ADF image of a single Au atom, e) calculated line scans for the gold atom potential, the probe, and a gold atom ADF image, f) line scan measurements of the Au atom intensity along perpendicular directions.

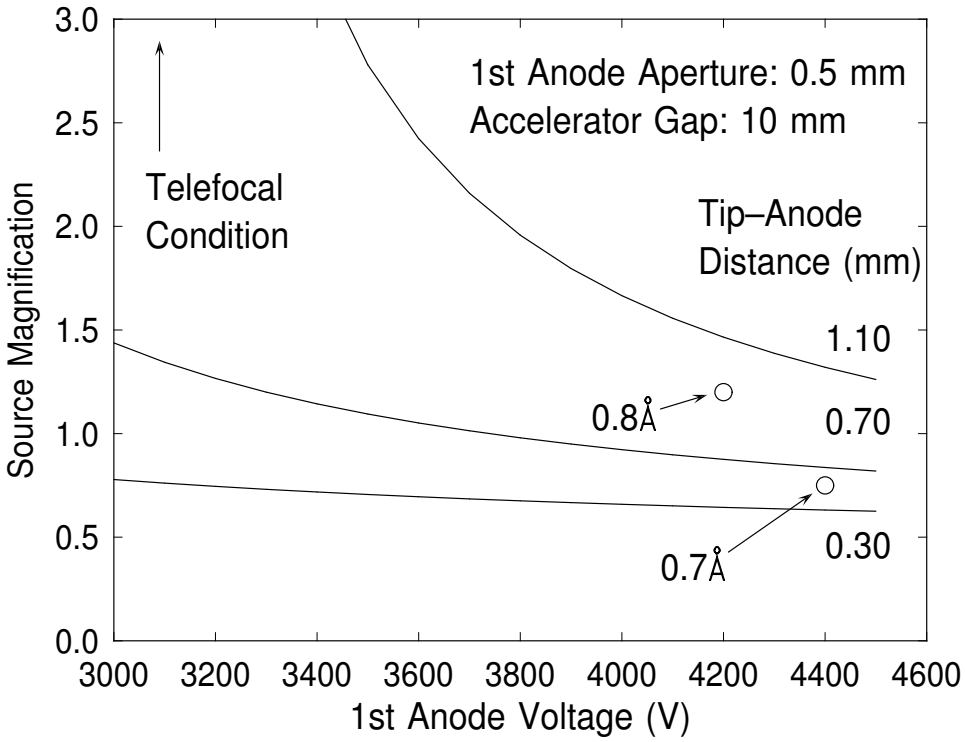

FIG. 4: Source magnification as a function of extraction voltage and separation between the tip and first anode for the VG Microscopes gun. Tip height variations as small at 0.2 mm can affect the source size by large amount for the lower extraction voltages.

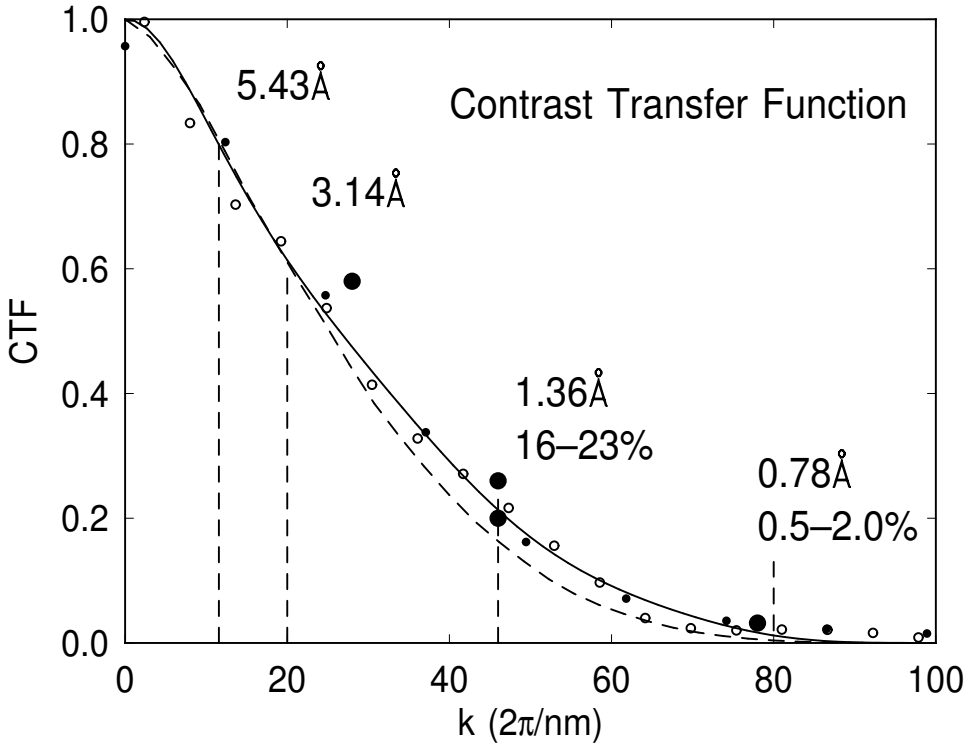

FIG. 5: Contrast Transfer Function for linear ADF imaging using the 0.8 Å diameter probe at Guassian focus. Clearly only a small part of the total contrast information is useful for answering questions about structure on the 0.8 Å length scale. Circles are measurements of contrast in Si [110] and [211] projections.

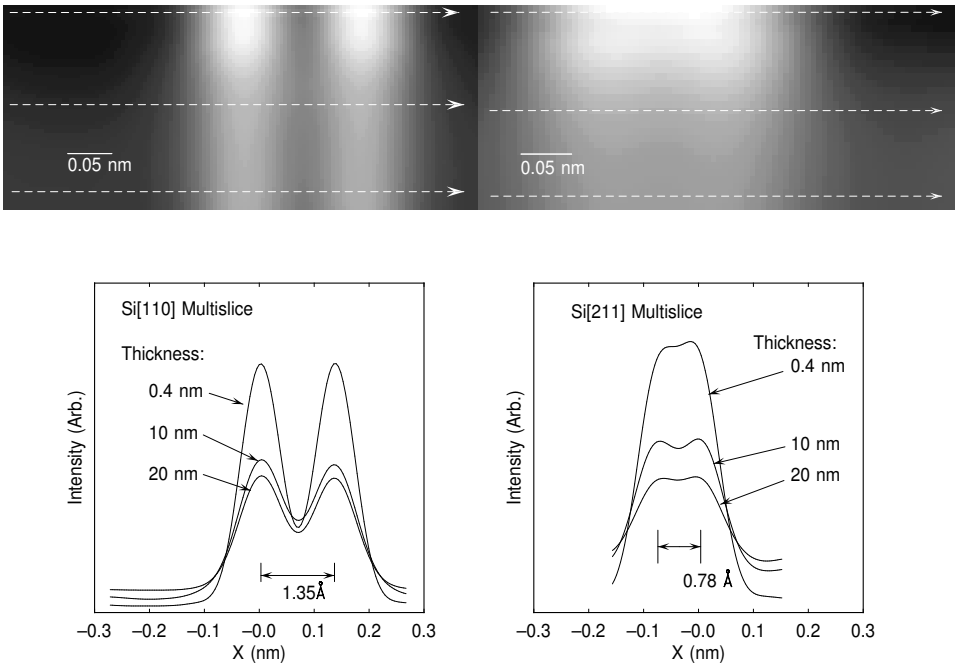

FIG. 6: Comparison of multislice ADF image calculations for the dumbbell structures in the Si[110] and [211] projections as a function of specimen thickness. In the [110] case, the dumbbell contrast decreases as the thickness increases, while the [211] dumbbell contrast remains relatively constant.

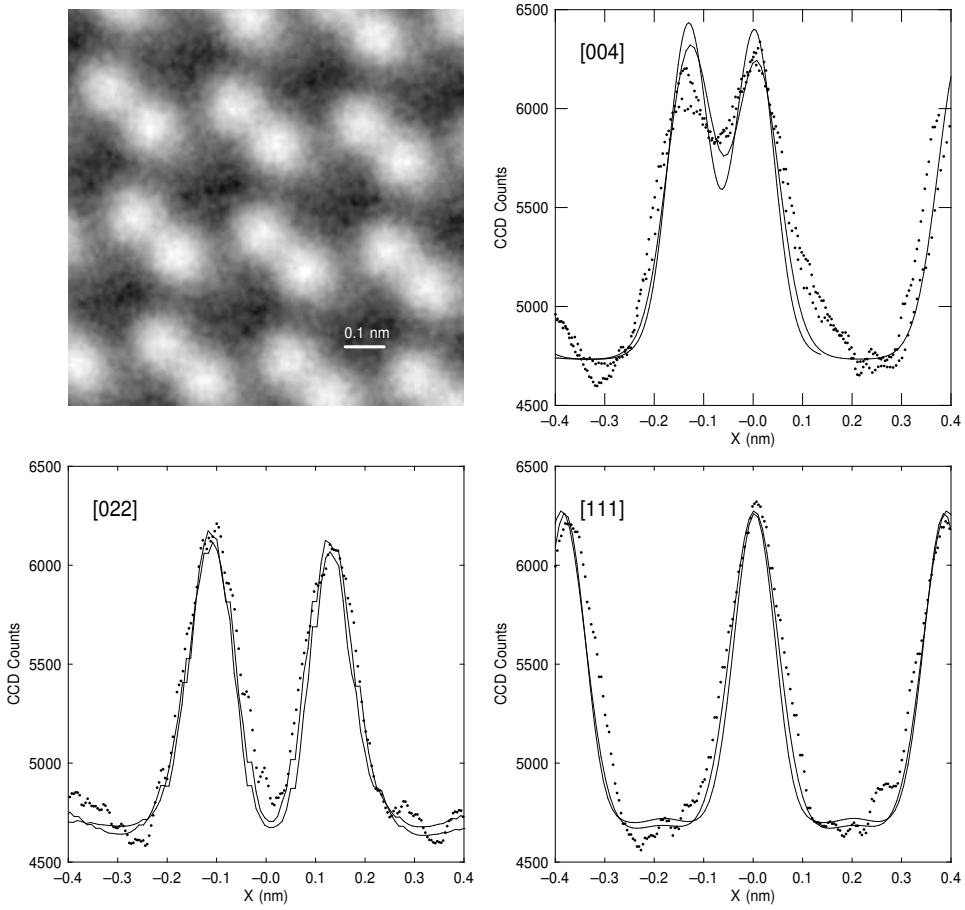

FIG. 7: Image and line scan data from Si[110], compared with multislice simulations using 0.05 and 0.08 nm source sizes. Agreement is good for the [111] and [220] type fringes at 0.05 nm source size, but the dumbbell [004] fringes are not well characterized by the calculation.

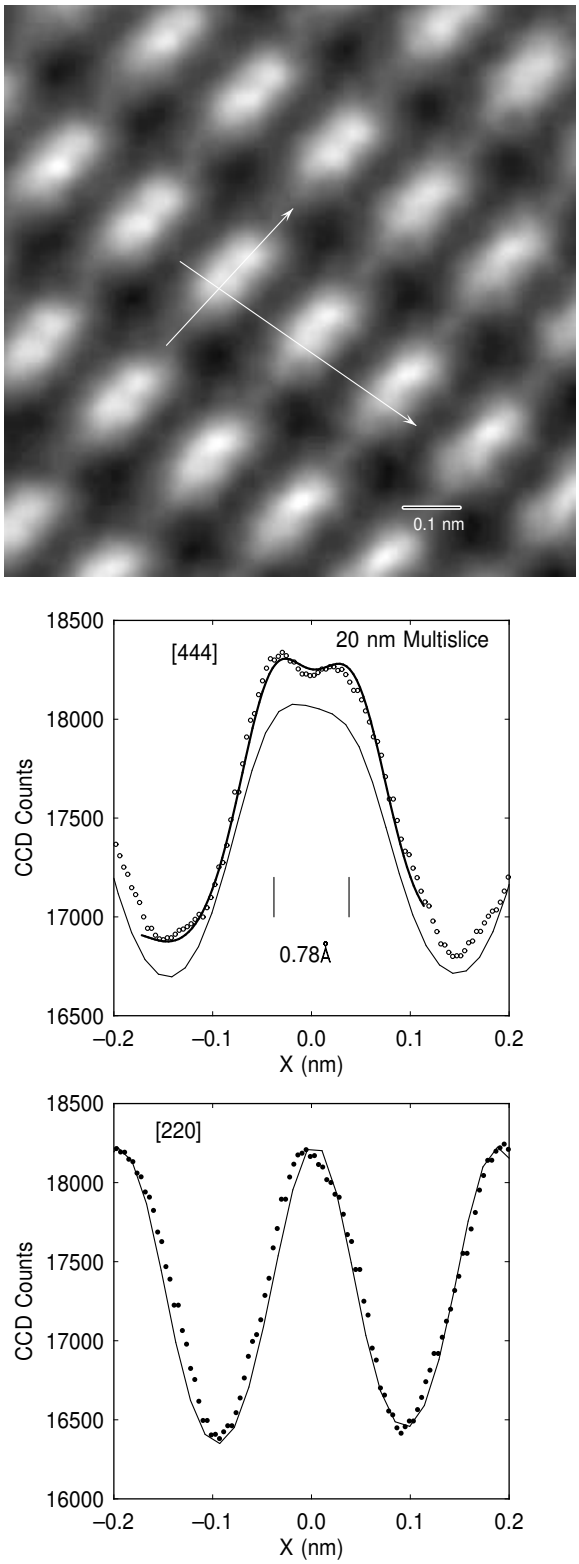

FIG. 8: Image and line scan data from Si[211], compared with multislice simulations using 0.05 and 0.08 nm source sizes. Agreement is good for both the [220] and the 0.78 Å[444] dumbbell fringes using a 0.05 nm source size. However, the [444] fringes would not be resolved using a 0.08 nm source.

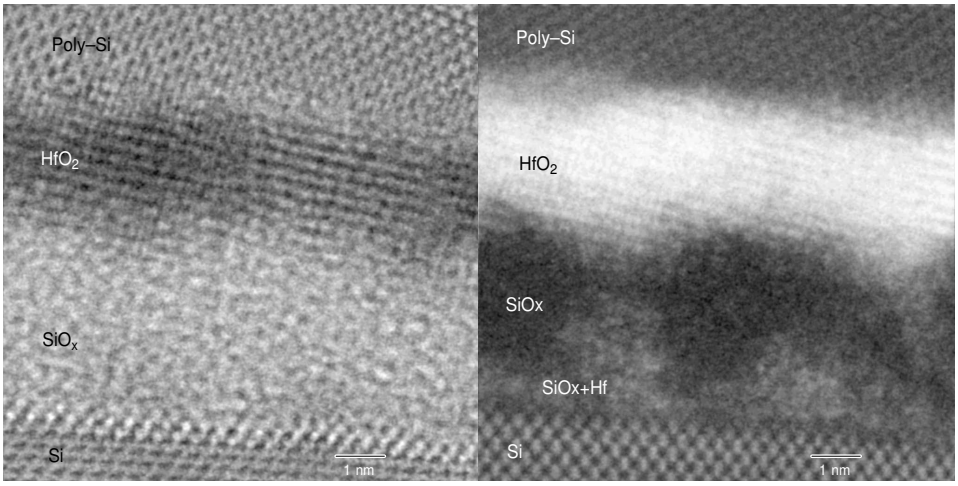

FIG. 9: BF-ADF image pair of a hi-K dielectric structure. Hf atoms within the SiO_x interface layer are readily visible in the ADF image. The images were acquired for 0.2 sec using a beam current of order 150 pA.

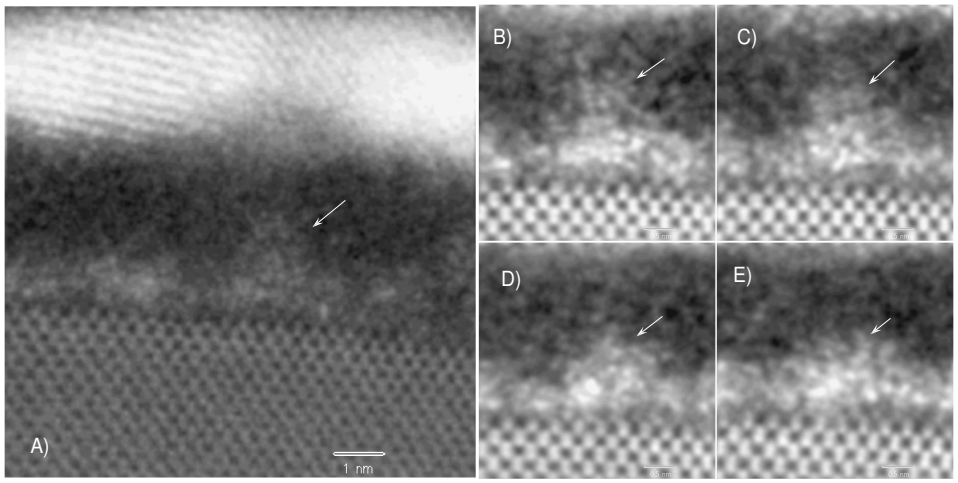

FIG. 10: ADF images of Hf atoms within the SiO_x interface layer between HfO_x and Si substrate of a hi-K gate insulator structure. The images were integrated for 0.2 sec at intervals of 1 sec.